ISBN: 978-628-96613-3-0. ISSN: 2414-6390. Digital Object Identifier: https://dx.doi.org/10.18687/LACCEI2026.1.1.945

First-Principles Investigation of the Semiconducting Behavior in Hybrid $CH_3NH_3PbBr_3$ Perovskite Using the Quantum ESPRESSO Suite

J. Peñalva, PhD *, J. Bolaños, Msc † and R. Larico, PhD ‡

*Faculty of Engineering, Universidad Tecnológica del Perú, Lima, Peru
†Faculty of Engineering, Universidad Tecnológica del Perú, Lima, Peru
‡ Universidade Federal do Pampa (UNIPAMPA), Itaqui-RS, Brazil

***Abstract*—This study explores the electronic and structural characteristics of cubic methylammonium lead bromide ($CH_3NH_3PbBr_3$) through Density Functional Theory (DFT) calculations performed with Quantum ESPRESSO. Following rigorous convergence benchmarks ($E_{cutwfc} = 45$ Ry, $E_{cutrho} = 300$ Ry, and a $3 \times 3 \times 3$ k-point grid), the simulated X-ray diffraction pattern is consistent with a single-phase cubic perovskite structure. Our results identify a direct band gap of 2.01 eV situated at the R high-symmetry point. Analysis of the Partial Density of States (PDOS) reveals that the Valence Band Maximum is primarily composed of Pb(s) and Br(p) states, while the Conduction Band Minimum is governed by Pb(p) anti-bonding orbitals. These findings underscore the material's suitability for optoelectronic devices operating in the visible spectrum ($\lambda \approx 617$ nm).**

***Keywords*—Hybrid perovskite, Density Functional Theory, Quantum ESPRESSO, Band gap engineering, Electronic structure, Optoelectronics.**

I. Introduction

Organic–Inorganic Hybrid Perovskites (OIHPs) have emerged over the past decade as one of the most scientifically compelling classes of materials [1]. This growing interest stems from their broad potential in next-generation optoelectronic devices, such as high-efficiency solar cells, light-emitting diodes (LEDs), and photodetectors, which has driven intense and sustained research activity in the field.

Within this family, Methylammonium Lead Bromide ($CH_3NH_3PbBr_3$, hereafter $MAPbBr_3$) stands out as a highly promising candidate for various applications, particularly in photovoltaic technology [2]. However, to fully optimize the performance of $MAPbBr_3$ based devices regarding their synthesis, properties, and scalability, it is essential to possess a fundamental and detailed understanding of their structural and electronic properties at the simulation level [2] [3]. The nature of its *band gap* and the orbital composition of its frontier bands (valence and conduction) are critical parameters that dictate its efficiency in photon absorption and emission [4].

The state of the art in hybrid perovskites, summarized in Table I, includes diverse theoretical and experimental studies on these materials. Research has focused on the electronic structure and *band gap* using DFT. Tauheed et al. [5] and Yu et al. [6] investigated the $MAPbX_3$ (X=I,Br) perovskite via DFT calculations, determining a direct band gap between 1.49 and 1.92 eV, respectively. In parallel, experimental research has validated the crystalline phases [7] and demonstrated the *tunability* of the *band gap* through halide substitution (e.g., Chlorine), achieving values ranging between 2.2 and 2.9 eV [8]. Other efforts have been directed toward improving stability, a key challenge for these materials, through eco-friendly synthesis and doping [9], or toward the development of more precise and efficient computational methods [10].

TABLE I
Summary of Relevant Research on Halide Perovskites

Authors	Bandgap	Research Summary
Tauheed et al. [5]	2.02 eV	DFT study of the electronic structure and mobility of pristine and fluorinated $MAPbX_3$ perovskites.
Yu et al. [6]	1.92 eV	DFT study (with vdW interactions) of the electronic properties of $CH_3NH_3PbX_3$ (X=I, Br), confirming direct *band gap* (1.49 eV for I, 1.92 eV for Br).
Jung et al. [7]	2.27 eV	Identification of the electronic structure and phases in $CH_3NH_3PbBr_3$ crystals. The band gap was measured using Raman spectroscopy.
Alvarez et al. [8]	2.2 - 2.9 eV	Investigation (SXRD) of $CH_3NH_3Pb(Br_{1-x}Cl_x)_3$ powders, demonstrating the band gap can be tuned (2.2–2.9 eV) by varying Cl concentration.
Nazim et al. [9]	2.33 eV	Development of an eco-friendly synthesis for Co-doped (Co^{2+}) $CH_3NH_3PbBr_3$ nanocrystals to improve stability.
Tao et al. [10]	2.40 eV	Proposes a method (DFT-1/2) to predict the *band gap* with accuracy similar to the GW method, but at a lower computational cost.
Rugut et al. [11]	1.49 eV	DFT study of the structural, mechanical, and optoelectronic properties of $CH_3NH_3PbI_3$, finding a direct *band gap* of $\sim$1.49 eV.

Despite recent advances, further computational study of the cubic phase of $CH_3NH_3PbBr_3$ remains necessary. Therefore, this work develops a systematic approach based on DFT calculations implemented in Quantum ESPRESSO, complemented by structural visualization with VESTA. The use of Cif2cell allows for efficient file transformation between both environments, enabling the definition of a clear and applicable methodology for future research on materials with optoelectronic potential, while also considering computational cost. In this context, the objective is to characterize the electronic properties based on the band structure and density of states, identifying the nature of the band gap and the orbital contribution.

II. Computational Methods

The simulation of the structural and electronic properties of cubic $MAPbBr_3$ perovskite was conducted using *first-principles* calculations based on DFT. The complete computational workflow is schematically illustrated in Figure 1. The initial cubic crystal structure of $MAPbBr_3$ was obtained from Crystallographic Information Files (CIF), which were subsequently visualized and analyzed using VESTA software [12]. Based on this structure, theoretical XRD patterns were simulated.

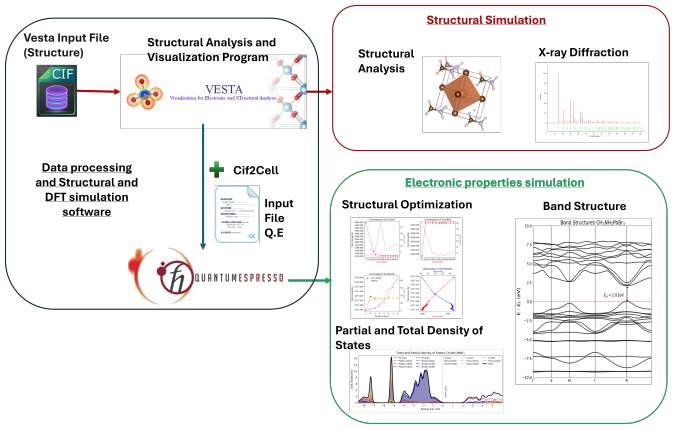

Fig. 1. Computational methodology workflow. The process starts with a CIF file, visualized in VESTA and converted by Cif2Cell for Q.E. The DFT workflow includes structural (XRD) and electronic property (band structure, DOS) analyses.

For the DFT calculations, the CIF files were processed using the Cif2Cell utility [13] in order to generate the appropriate input files for the Q.E. simulation package [14], [15]. All DFT calculations were carried out within the Q.E. framework, employing the Generalized Gradient Approximation (GGA) of Perdew-Burke-Ernzerhof (PBE) for the exchange-correlation functional, along with ultrasoft pseudopotentials to describe the electron-ion interactions. For the property analysis, a complete structural optimization (geometry relaxation) of both the lattice parameters and the internal atomic positions was performed, until the forces and energy were minimal in the structure. Following the relaxation, Self-Consistent Field (SCF) calculations were proceeded with to obtain the ground-state electron density. Finally, the electronic band structure and the total and partial Density of States (DOS) were calculated along high-symmetry points in the first Brillouin zone, thus allowing for the analysis of the electronic characteristics and the *band gap* (E_g) of the materials.

III. Results

A. Structural Model and Simulated XRD Pattern of $CH_3NH_3PbBr_3$

The structural analysis focused on the cubic phase of the methylammonium lead bromide perovskite ($CH_3NH_3PbBr_3$). As illustrated in the inset of Figure 2, the structure adopts the archetypal ABX_3 perovskite architecture. The crystal lattice is defined by a three-dimensional framework formed by corner-sharing $[PbBr_6]^{4-}$ octahedra (containing the B and X sites). The organic methylammonium cation ($CH_3NH_3^+$) occupies the A site, located within the large interstitial void formed by this octahedral cage. This high-symmetry cubic configuration, visualized with VESTA, is fundamental for understanding the electronic and optical properties of the material and served as a validated starting point for the subsequent DFT calculations.

To validate the crystal structure and provide a reference for experimental characterization, the XRD pattern was simulated from the optimized unit cell. Figure 2 shows the theoretical diffractogram, which exhibits a series of sharp and well-defined Bragg peaks. This sharpness is indicative of a high degree of crystallinity and long-range order. The principal reflections in the XRD pattern are located at the following 2θ angles and correspond to the indicated crystallographic planes (Miller indices).

The three most intense reflections are observed at approximately $\mathbf{15}^\circ$, $\mathbf{30}^\circ$, and $\mathbf{34}^\circ$, which are indexed and correspond to the crystallographic planes $(\mathbf{001})$, $(\mathbf{002})$, and $(\mathbf{012})$, respectively. This simulated pattern serves as an essential computational "fingerprint" for phase identification and purity confirmation of experimentally synthesized $CH_3NH_3PbBr_3$ samples.

B. Energy Convergence Tests and Structural Optimization

Before proceeding with the calculation of the electronic properties, a systematic convergence study was carried out to determine the optimal computational parameters for the DFT simulations of $CH_3NH_3PbBr_3$ with Q.E. This step is critical to ensure that the results are computationally efficient and, at the same time, physically precise, minimizing the numerical errors associated with the convergence of the cutoff energy and the density of the k-point mesh. Figure 3 summarizes the results of these convergence tests.

First, the wavefunction cutoff energy (*Ecutwfc*) was determined. Figure 3(a) shows the total energy of the system as a function of *Ecutwfc*, where it is observed that the energy

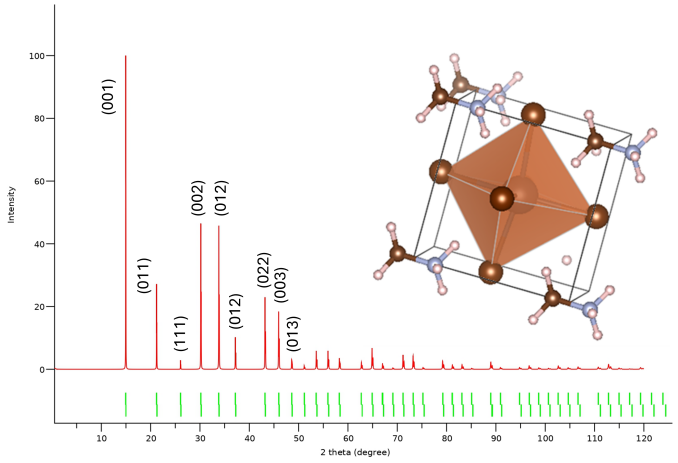

Fig. 2. Simulated XRD pattern of cubic $CH_3NH_3PbBr_3$ generated via VESTA. It serves as a high-crystallinity phase reference, highlighting main Bragg reflections at 15°, 30°, and 34°. The inset depicts the ABX_3 unit cell, showing $CH_3NH_3^+$ cations occupying the voids within the corner-sharing $PbBr_6$ octahedral framework.

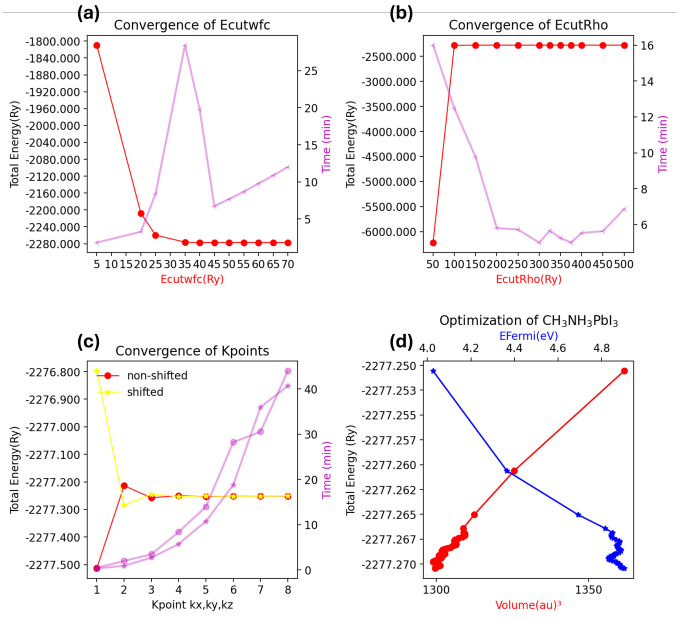

Fig. 3. Convergence studies of key DFT parameters for $CH_3NH_3PbBr_3$ calculations. (a) Convergence of wavefunction cutoff energy (*Ecutwfc*), converging at 45 Ry. (b) Convergence of charge density cutoff energy (*EcutRho*), set at 300 Ry. (c) Convergence of k-point mesh density, stabilizing with a $3 \times 3 \times 3$ mesh. (d) Optimization of the unit cell volume to find the equilibrium state.

converges (i.e., stops varying significantly) starting from 45 Ry. Based on this, that value was selected. Subsequently, convergence was performed for the charge density cutoff energy (*EcutRho*), establishing a value of 300 Ry (Figure 3(b)). Next, convergence with respect to the density of the k-point mesh in the Brillouin zone was evaluated. As illustrated in Figure 3(c), the total energy stabilizes with a Monkhorst-Pack mesh of $3\times3\times3$, which was selected for the structural optimization and electronic properties calculations.

Using the converged cutoff parameters and k-point mesh (45 Ry, 300 Ry, and $3\times3\times3$), a complete optimization of the unit cell geometry ('vc-relax' calculation) was performed. Figure 3(d) displays the total energy variation as a function of the cell volume. The structural optimization required to achieve the minimum energy configuration (ground state) was performed using the BFGS (Broyden–Fletcher–Goldfarb–Shanno) minimization algorithm. This method iteratively minimizes the system's total energy by reducing the Hellmann-Feynman forces on the ions and the Nielsen-Martin stress tensor on the unit cell [16], [17]. The resulting optimized structure defines the equilibrium volume and the material's theoretical lattice parameter in its ground state, corresponding to the minimum energy achieved by the convergence of the algorithm.

This fully relaxed structure served as the starting point for all subsequent calculations, including the determination of the band structure and the density of states.

C. Total and Partial Density of States (TDOS/PDOS) Analysis

Once the equilibrium geometric structure was obtained, the Total Density of States (TDOS) and the Partial Density of States (PDOS) were calculated to determine the orbital composition of the electronic bands. Figure 4 presents the TDOS (black line) and the PDOS projected onto the different atoms and their orbitals for the $CH_3NH_3PbBr_3$ compound. The Fermi level (E_F), which separates the occupied states (valence band) from the vacant states (conduction band), has been set to 0 eV. The results confirm the semiconductor nature of the material, evidenced by a clear *band gap* where the density of states is zero.

The detailed PDOS analysis reveals the composition of the Valence Band Maximun (VBM). The top part of the valence band, from approximately -4.3 eV up to the Fermi level (0 eV), is predominantly formed by Br$(4p)$ orbitals (blue shaded area). In this same region, there is a significant contribution from Pb$(6s)$ orbitals. This hybridization between the Pb$(6s)$ and Br$(4p)$ orbitals is characteristic of lead halide perovskites and gives rise to the anti-bonding character of the VBM. Additionally, a sharp, localized peak is observed in the deep valence band, near -5.2 eV, which originates almost exclusively from Pb$(6p)$ orbitals, corresponding to the lead's 'p' lone pair state. States associated with the organic cation (C$(2p)$, N$(2p)$, and H$(1s)$) are found in even deeper valence bands (below -6 eV), indicating that they do not participate directly in the formation of the valence band edge.

Above the Fermi level, the Conduction Band Minimum (CBM) and the bottom part of the conduction band (from approx. 2 eV up to 6 eV) are dominated by the Pb$(6p)$ orbitals (red dots). In this same range, minor contributions from Br$(4p)$ and the organic cation's orbitals appear at much higher energies. This PDOS analysis confirms that the fundamental optoelectronic properties of $CH_3NH_3PbBr_3$ are governed by

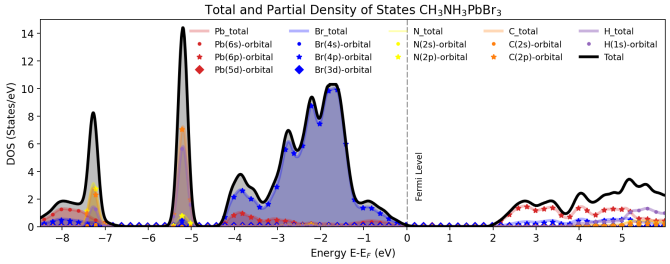

Fig. 4. The Partial Density of States (PDOS) analysis for $CH_3NH_3PbBr_3$ confirms the optoelectronic dominance of the $PbBr_6$ framework. The VBM is formed by hybrid Br($4p$) and Pb($6s$) orbitals, while the Conduction Band is dominated by Pb($6p$) states. Organic cation orbitals (C($2p$)/N($2p$)/H($1s$)) are localized in deep valence bands (≈ -5.2 eV), showing minimal contribution to the *band gap* edge.

the inorganic anion $[PbBr_6]^{4-}$. Specifically, the *band gap* transition occurs between the hybrid Pb($6s$) − Br($4p$) states of the VBM and the Pb($6p$) states of the CBM, while the methylammonium molecule ($CH_3NH_3^+$) primarily acts as a structural spacer, due to the fact that it does not participate directly in the formation of the electronic states that define the forbidden band (VBM and CBM), limiting its function almost exclusively to the geometric support of the unit cell.

D. Band Structure and TDOS

To evaluate the optoelectronic potential of the $CH_3NH_3PbBr_3$ perovskite, its electronic band structure and density of states (DOS/PDOS) were calculated, as presented in Figure 5. The band structure was plotted along the high-symmetry paths ($\Gamma \to X \to M \to \Gamma \to R \to X$) in the first Brillouin zone, with the Fermi level (E_F) adjusted to 0 eV. The analysis reveals that the VBM and the CBM are concurrently located at the high-symmetry point R. This alignment confirms that the $CH_3NH_3PbBr_3$ in its cubic phase is a direct band gap semiconductor. The calculated *band gap* value at this point is $E_g = 2.01$ eV. This direct gap nature is highly desirable for photovoltaic and light-emitting diode (LED) applications, as it allows for efficient electronic transitions (absorption and emission of photons).

The analysis of the PDOS is shown on the right side of Figure 5, which provides a fundamental vision of the orbital composition of the frontier bands. It is confirmed that the VBM (upper edge of the valence band) is predominantly formed by a hybridization of the Pb($6s$) and Br($4p$) orbitals. Conversely, the CBM (lower edge of the conduction band) is dominated almost exclusively by the Pb($6p$) orbitals. The PDOS also demonstrates that the states associated with the organic cation (C, N, H) are localized in deep valence bands (mainly between -5 eV and -10 eV), far below the Fermi level. This indicates that the methylammonium molecule acts primarily as a structural spacer, while the optoelectronic properties in the *band gap* are governed by the inorganic anion $[PbBr_6]^{4-}$.

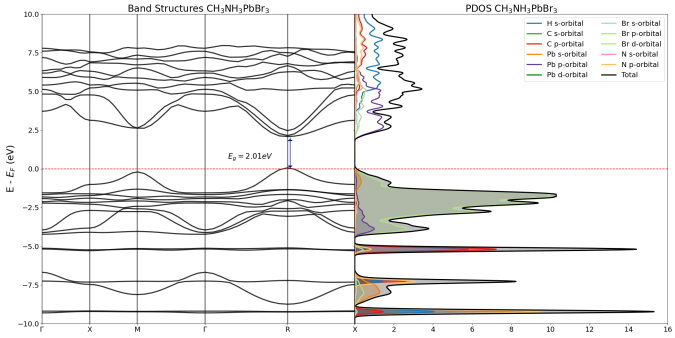

Fig. 5. The DFT-calculated band structure for $CH_3NH_3PbBr_3$ reveals a direct *band gap* ($E_g = 2.01$ eV), confirmed by the VBM and CBM coinciding at the R point of the Brillouin Zone. The PDOS analysis shows that the frontier bands are governed by the $PbBr_6$ inorganic framework, with the VBM formed by hybrid Pb(s) and Br(p) states, and the CBM dominated by Pb(p) orbitals, underscoring the material's potential for optoelectronic applications.

IV. Discussion of Results

A. Analysis of Structural and Electronic Properties

The simulated XRD pattern of the $CH_3NH_3PbBr_3$ perovskite in its cubic structural phase shows sharp and well-defined Bragg peaks, notably in the (001), (002), (012), and (011) orientations, along with others of lower intensity, which is characteristic of high crystallinity (Figure 2). These orientations are in agreement with experimental results obtained by Evans et al. [18]. This pattern serves as a computational "fingerprint" that provides the starting structure for DFT calculations and validates the experimental XRD results.

The analysis of the PDOS, detailed in Figure 4 and projected in Figure 5, is of great importance for understanding the optical properties of the perovskite under study, above the Fermi level, the CBM and the lower conduction region (2–6 eV) are mainly composed of Pb($6p$) states. Minor contributions from Br(4p) and organic orbitals appear only at higher energies. This indicates that the optoelectronic response is mainly controlled by the inorganic $[PbBr_6]^{4-}$ framework [6].

The central result of this research is the determination of the electronic band structure, shown in Figure 5. The analysis reveals that the $CH_3NH_3PbBr_3$ perovskite in its cubic phase possesses a *direct band gap* with a calculated value of $E_g = 2.01$ eV, which is consistent with previous experimental and theoretical results, see Table II.

The direct nature of the *band gap* ($E_g = 2.01$ eV) is highly relevant for optoelectronic applications of the perovskite. A direct *band gap* provides information about electronic transitions (photon absorption and emission). The obtained E_g value (2.01 eV) corresponds to a cutoff wavelength ($\lambda_c = hc/E_g$) of approximately 617 nm, within the visible spectrum (orange-red). This places the absorption edge firmly within the visible range, allowing $CH_3NH_3PbBr_3$ to absorb photons with sufficient energy to excite electrons from the valence band to the conduction band, effectively making it a conductive

material. This result makes it an ideal candidate as a visible-light absorber and electron generator for solar cell applications.

Our theoretical results are compared with previous studies in Table II. The *band gap* of 2.01 eV was obtained using the GGA-PBE exchange and correlation functional, and is consistent with reported theoretical and experimental values, which range between 1.49 and 2.02 eV. This variation of bandgaps is mainly due to simulation factors such as the choice of exchange-correlation functional (PBE, PBEsol, HSE06), the inclusion of relativistic effects and spin-orbit coupling (SOC), the k-point mesh density, the plane-wave cutoff energy, and the orientation of the $CH_3NH_3^+$ cation. On the other hand, experimental *band gap* values ranging from 2.2 to 2.35 eV may differ due to synthesis methods, defects, grain size, quantum confinement, and measurement conditions. Our result falls within the expected range, validating the reliability of the DFT approach employed.

TABLE II
COMPARISON OF CALCULATED AND EXPERIMENTAL BAND GAPS FOR $CH_3NH_3PbBr_3$ (LITERATURE REVIEW)

Ref.	**Structure**	**Theor.** E_g	**Exp./Ref.** E_g
[5]	cubic	2.02 eV	2.23, 2.35 eV
[8]	cubic	-	2.2 eV
[7]	cubic	-	2.27 eV
[9]	cubic	-	2.33 eV
[6]	pseudo-cubic	1.92 eV	2.2 eV, 2.25 eV
[11]	pseudo-cubic	1.49 eV	-
[10]	pseudo cubic	2.40 eV	2.33–2.35 eV

V. CONCLUSION

In this work, the cubic phase of $CH_3NH_3PbBr_3$ was analyzed via first-principles calculations to characterize its electronic behavior. The simulated diffraction pattern agrees with experimental signatures, supporting the structural model. Convergence analysis was essential to guarantee dependable computational results.

Our analysis shows that $CH_3NH_3PbBr_3$ exhibits a direct gap at the R point, with an energy of approximately 2.01 eV. The band-edge states are largely dominated by the octahedral Pb-Br network. As a result, the absorption onset falls in the visible spectrum, which is favorable for solar energy conversion.

Finally, the comparison with previous studies shows that the *band gap* obtained in this work lies within the range reported in the literature, both for theoretical simulations and experimental measurements. This agreement confirms that our result is consistent with previous studies. Overall, these results validate the reliability of the DFT approach employed and highlight the potential of $CH_3NH_3PbBr_3$ for photovoltaic and optoelectronic applications.

ACKNOWLEDGMENT

This work was supported by the Private University under Rectoral Resolution "RR Nº 0085-2024-R-UTP Proyectos I+D 2024 Lima". The authors acknowledge this support, which enabled the research presented in this paper.

REFERENCES

[1] Y. Zhao and K. Zhu, "Organic–inorganic hybrid lead halide perovskites for optoelectronic and electronic applications," *Chem. Soc. Rev.*, vol. 45, pp. 655–689, 2016. [Online]. Available: http://dx.doi.org/10.1039/C4CS00458B

[2] R. Zhang, W. Cai, T. Bi, N. Zarifi, T. Terpstra, C. Zhang, Z. V. Verdeny, E. Zurek, and S. Deemyad, "Effects of nonhydrostatic stress on structural and optoelectronic properties of methylammonium lead bromide perovskite," *The Journal of Physical Chemistry Letters*, vol. 8, no. 15, pp. 3457–3465, 2017, pMID: 28691486. [Online]. Available: https://doi.org/10.1021/acs.jpclett.7b01367

[3] H. Xue, G. Brocks, and S. Tao, "Intrinsic defects in primary halide perovskites: A first-principles study of the thermodynamic trends," *Phys. Rev. Mater.*, vol. 6, p. 055402, May 2022. [Online]. Available: https://link.aps.org/doi/10.1103/PhysRevMaterials.6.055402

[4] J. Endres, D. A. Egger, M. Kulbak, R. A. Kerner, L. Zhao, S. H. Silver, G. Hodes, B. P. Rand, D. Cahen, L. Kronik, and A. Kahn, "Valence and conduction band densities of states of metal halide perovskites: A combined experimental–theoretical study," *The Journal of Physical Chemistry Letters*, vol. 7, no. 14, pp. 2722–2729, 2016, pMID: 27364125. [Online]. Available: https://doi.org/10.1021/acs.jpclett.6b00946

[5] M. T. Ilyas, K. Kaur, J. Sharma, and G. S. S. Saini, "Dft study of electronic structure and mobility of pristine and fluorinated methylammonium lead halide perovskites (ch3nh3pbx3, x = i, br, cl)," *International Journal of Energy Research*, vol. 46, no. 5, pp. 6889–6900, 2022. [Online]. Available: https://onlinelibrary.wiley.com/doi/abs/10.1002/er.7623

[6] C.-J. Yu, U.-G. Jong, M.-H. Ri, G.-C. Ri, and Y.-H. Pae, "Electronic structure and photoabsorption property of pseudocubic perovskites ch3nh3pbx3(x = i, br) including van der waals interaction," *Journal of Materials Science*, vol. 51, 11 2016.

[7] H. R. Jung, G. Y. Kim, B. P. Nguyen, H.-J. Jin, W. Jo, T. T. Thu Nguyen, S. Yoon, W. S. Woo, C. W. Ahn, S. Cho, and I. W. Kim, "Optical and scanning probe identification of electronic structure and phases in ch3nh3pbbr3 crystal," *The Journal of Physical Chemistry C*, vol. 121, no. 40, pp. 21 930–21 934, 2017. [Online]. Available: https://doi.org/10.1021/acs.jpcc.7b06765

[8] M. C. Alvarez-Galván, J. A. Alonso, C. A. López, E. López-Linares, C. Contreras, M. J. Lázaro, F. Fauth, and M. V. Martínez-Huerta, "Crystal growth, structural phase transitions, and optical gap evolution of ch3nh3pb(br1–xclx)3 perovskites," *Crystal Growth & Design*, vol. 19, no. 2, pp. 918–924, 2019. [Online]. Available: https://doi.org/10.1021/acs.cgd.8b01463

[9] M. Nazim, A. A. Parwaz Khan, F. Khan, S. K. Cho, and R. Ahmad, "Insertion of metal cations into hybrid organometallic halide perovskite nanocrystals for enhanced stability: eco-friendly synthesis, lattice strain engineering, and defect chemistry studies," *Nanoscale Adv.*, vol. 4, pp. 2729–2743, 2022. [Online]. Available: http://dx.doi.org/10.1039/D2NA00053A

[10] S. X. Tao, X. Cao, and P. A. Bobbert, "Accurate and efficient band gap predictions of metal halide perovskites using the dft-1/2 method: Gw accuracy with dft expense," *Scientific Reports*, vol. 7, no. 1, p. 14386, Oct 2017. [Online]. Available: https://doi.org/10.1038/s41598-017-14435-4

[11] E. K. Rugut, N. E. Maluta, R. R. Maphanga, R. E. Mapasha, and J. K. Kirui, "Structural, mechanical, and optoelectronic properties of ch3nh3pbi3 as a photoactive layer in perovskite solar cell," *Photonics*, vol. 11, no. 4, 2024. [Online]. Available: https://www.mdpi.com/2304-6732/11/4/372

[12] K. Momma and F. Izumi, "Vesta3 for three-dimensional visualization of crystal, volumetric and morphology data," *Journal of Applied Crystallography*, vol. 44, no. 6, pp. 1272–1276, 2011. [Online]. Available: https://onlinelibrary.wiley.com/doi/abs/10.1107/S0021889811038970

[13] T. Björkman, "Cif2cell: Generating geometries for electronic structure programs," *Computer Physics Communications*, vol. 182, no. 5, pp. 1183–1186, 2011. [Online]. Available: https://www.sciencedirect.com/science/article/pii/S0010465511000336

[14] P. Giannozzi, S. Baroni, N. Bonini, M. Calandra, R. Car, C. Cavazzoni, D. Ceresoli, G. L. Chiarotti, M. Cococcioni, I. Dabo, A. Dal Corso, S. de Gironcoli, S. Fabris, G. Fratesi, R. Gebauer, U. Gerstmann,

C. Gougoussis, A. Kokalj, M. Lazzeri, L. Martin-Samos, N. Marzari, F. Mauri, R. Mazzarello, S. Paolini, A. Pasquarello, L. Paulatto, C. Sbraccia, S. Scandolo, G. Sclauzero, A. P. Seitsonen, A. Smogunov, P. Umari, and R. M. Wentzcovitch, "Quantum espresso: a modular and open-source software project for quantum simulations of materials," *Journal of Physics: Condensed Matter*, vol. 21, no. 39, p. 395502, sep 2009. [Online]. Available: https://doi.org/10.1088/0953-8984/21/39/395502

[15] P. Giannozzi, O. Andreussi, T. Brumme, O. Bunau, M. Buongiorno Nardelli, M. Calandra, R. Car, C. Cavazzoni, D. Ceresoli, M. Cococcioni, N. Colonna, I. Carnimeo, A. Dal Corso, S. de Gironcoli, P. Delugas, R. A. DiStasio, A. Ferretti, A. Floris, G. Fratesi, G. Fugallo, R. Gebauer, U. Gerstmann, F. Giustino, T. Gorni, J. Jia, M. Kawamura, H.-Y. Ko, A. Kokalj, E. Küçükbenli, M. Lazzeri, M. Marsili, N. Marzari, F. Mauri, N. L. Nguyen, H.-V. Nguyen, A. Otero-de-la Roza, L. Paulatto, S. Poncé, D. Rocca, R. Sabatini, B. Santra, M. Schlipf, A. P. Seitsonen, A. Smogunov, I. Timrov, T. Thonhauser, P. Umari, N. Vast, X. Wu, and S. Baroni, "Advanced capabilities for materials modelling with quantum espresso," *Journal of Physics: Condensed Matter*, vol. 29, no. 46, p. 465901, oct 2017. [Online]. Available: https://doi.org/10.1088/1361-648X/aa8f79

[16] O. H. Nielsen and R. M. Martin, "Quantum-mechanical theory of stress and force," *Phys. Rev. B*, vol. 32, pp. 3780–3791, Sep 1985. [Online]. Available: https://link.aps.org/doi/10.1103/PhysRevB.32.3780

[17] R. M. Wentzcovitch, "Invariant molecular-dynamics approach to structural phase transitions," *Phys. Rev. B*, vol. 44, pp. 2358–2361, Aug 1991. [Online]. Available: https://link.aps.org/doi/10.1103/PhysRevB.44.2358

[18] P. E. Evans, M. Pink, A. A. Zhumekenov, G. Hao, Y. Losovyj, O. M. Bakr, P. A. Dowben, and A. J. Yost, "Rotationally free and rigid sublattices of the single crystal perovskite ch3nh3pbbr3 (001): The case of the lattice polar liquid," *The Journal of Physical Chemistry C*, vol. 122, no. 44, pp. 25 506–25 514, 2018. [Online]. Available: https://doi.org/10.1021/acs.jpcc.8b08994